CrossMark

ORIGINAL ARTICLE

Biomechanics of the classic metaphyseal lesion: finite element analysis

Andy Tsai[1] · Brittany Coats[2] · Paul K. Kleinman[1]

Abstract

Background The classic metaphyseal lesion (CML) is strongly associated with infant abuse, but the biomechanics responsible for this injury have not been rigorously studied. Radiologic and CT-pathological correlates show that the distal tibial CML always involves the cortex near the subperiosteal bone collar, with variable extension of the fracture into the medullary cavity. Therefore, it is reasonable to assume that the primary site of bone failure is cortical, rather than intramedullary.

Objective This study focuses on the strain patterns generated from finite element modeling to identify loading scenarios and regions of the cortex that are susceptible to bone failure.

Materials and methods A geometric model was constructed from a normal 3-month-old infant's distal tibia and fibula. The model's boundary conditions were set to mimic forceful manipulation of the ankle with eight load modalities (tension, compression, internal rotation, external rotation, dorsiflexion, plantar flexion, valgus bending and varus bending).

Results For all modalities except internal and external rotation, simulations showed increased cortical strains near the subperiosteal bone collar. Tension generated the largest magnitude of cortical strain (24%) that was uniformly distributed near the subperiosteal bone collar. Compression generated the same distribution of strain but to a lesser magnitude overall (15%). Dorsiflexion and plantar flexion generated high (22%) and moderate (14%) localized cortical strains, respectively, near the subperiosteal bone collar. Lower cortical strains resulted from valgus bending, varus bending, internal rotation and external rotation (8–10%). The highest valgus and varus bending cortical strains occurred medially.

Conclusion These simulations suggest that the likelihood of the initial cortical bone failure of the CML is higher along the margin of the subperiosteal bone collar when the ankle is under tension, compression, valgus bending, varus bending, dorsiflexion and plantar flexion, but not under internal and external rotation. Focal cortical strains along the medial margins of the subperiosteal bone collar with varus and valgus bending may explain the known tendency for focal distal tibial CMLs to occur medially. Further research is needed to determine the threshold of applied forces required to produce this strong indicator of infant abuse.

Introduction

The classic metaphyseal lesion (CML), described by Silverman in 1953 and detailed by Caffey in 1957, is regarded as a strong indicator of infant abuse [1–5]. Biomechanical study may offer insights into the nature of the events producing this distinctive injury. Since in vivo biomechanical experiments are not feasible, some studies have produced radiologically similar appearing fractures in deceased animal models, but histological confirmation of the CML pattern was not reported in these papers [6–8]. Even if the injury is eventually

✉ Andy Tsai
andy.tsai@childrens.harvard.edu

1 Department of Radiology, Harvard Medical School,
Boston Children's Hospital,
300 Longwood Ave., Boston, MA 02115, USA

2 Department of Mechanical Engineering,
University of Utah,
Salt Lake City, UT, USA

replicated in animal models, species differences, the use of cadaveric material and other methodological challenges could limit inferences made to the human infant.

Finite element modeling is a numerical technique that has been applied to study bone integrity and osteoporotic fractures [9–11]. Using biofidelic infant bone models and applying a variety of loads designed to simulate injury scenarios, finite element modeling has the potential to improve our understanding of CML biomechanics in the setting of abuse. Since the distal tibia is a common location for the CML [12], and the osseous geometry is a relatively symmetrical mildly flared cylinder, this was selected as a suitable site for finite element modeling.

Radiologic-histopathological correlation studies have shown that the distal tibial CML is a planar fracture extending from the junction of the bony cortex and subperiosteal bone collar centrally into the metaphyseal spongiosa [12–16]. Diffuse injuries may extend completely across the bone, separating a metaphyseal/epiphyseal fragment, leaving the physis intact [17]. Commonly, the lesions are focal, undercutting an arc of the subperiosteal bone collar and adjacent primary spongiosa (Fig. 1). One radiologic-histopathological study has demonstrated a tendency for the CML to favor the medial metaphyseal margin [12]. Although these radiologic-histopathological correlations suggest that the distal tibial CML is initiated at the junction of the cortex and subperiosteal bone collar, experimental biomechanical support for this view is lacking. This study employs microcomputed tomography (micro-CT) and finite element analysis of a human infant distal tibia under various loading scenarios to assess cortical strain patterns and identify potential sites of cortical bone failure occurring with the distal tibial CML.

Materials and methods

This study was exempt from institutional review board and HIPPA regulations because living human subjects and personal health information were not utilized.

Geometry

For anatomical fidelity, the geometry of our finite element model was derived from micro-CT data of a 3-month-old infant's left distal tibia and fibula. Abusive head trauma and homicide were reported as the cause and manner of death, respectively. Skeletal specimens, including the left distal tibia and fibula, were removed in the customary fashion at autopsy to assist the medical examiner's investigation [18]. The left distal tibia/fibula block specimen was initially preserved in formalin, removed from the formalin for all imaging (digital radiography, micro-CT), then decalcified and embedded in paraffin. The block was then sectioned with a microtome and stained with hematoxylin and eosin. Micro-CT was performed using an isotropic resolution of 45 μm^3 (Siemens MicroCAT II, Knoxville, TN) employing the following parameters: 45 kV, 500 μA, and 4,000 ms exposure time. To increase the signal-to-noise ratio of the data, we chose 2×2 detector binning and a modified Feldkamp algorithm for data reconstruction. Specimen radiography prior to micro-CT and subsequent histological assessment revealed normal distal tibial and fibular anatomy.

The focus of our finite element analysis was on the cortex of the distal tibia, but the underlying medullary cavity was included in the model to provide a more robust analysis. For numerical tractability, we considered the medullary cavity as a single
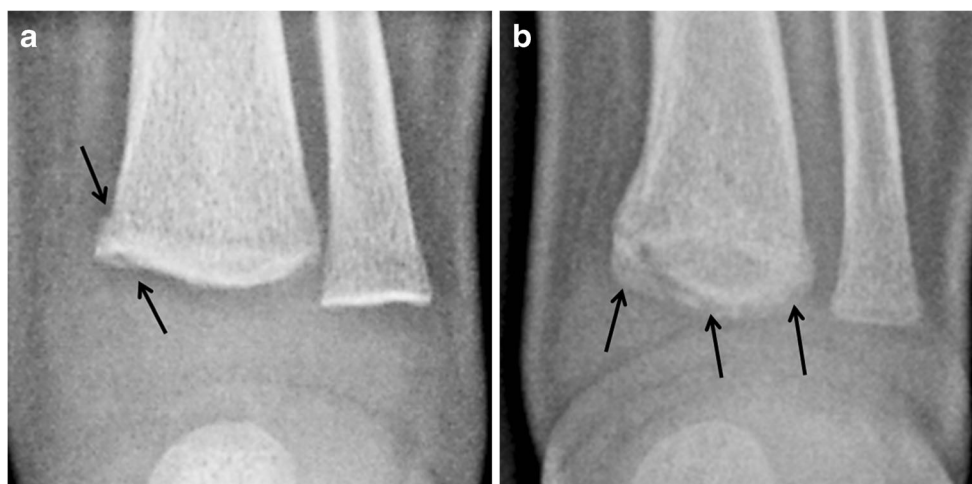

Fig. 1 Classic metaphyseal lesion in a 1-month-old boy with an acute right femoral shaft fracture and no history of trauma. Skeletal survey revealed multiple rib fractures and CMLs in different stages of healing. AP radiograph of the distal left tibia and fibula (**a**) demonstrates an oblique linear radiolucency (*arrows*) extending along the medial margin of the distal tibial metaphysis resulting in a corner fracture pattern. Follow-up imaging 2 weeks later (**b**) now shows a bucket handle pattern with marginal sclerosis (*arrows*); the fracture fragment remains most conspicuous medially

structural unit with a single set of material properties. The finite element geometry was derived by segmenting out the bony cortices and medullary cavities of the distal tibia and fibula from micro-CT data using intensity thresholding, region growing, Gaussian smoothing and manual adjustment (ScanIP; Simpleware Ltd., Exeter, UK). The final 318 × 480 × 324 voxel model was 14.31 × 21.60 × 14.58 mm in size (Fig. 2). The volumes of the distal tibial and fibular cortices were 288.94 mm^3 and 151.74 mm^3, respectively, and the volumes of the medullary cavities were 1,007.60 mm^3 and 158.73 mm^3, respectively.
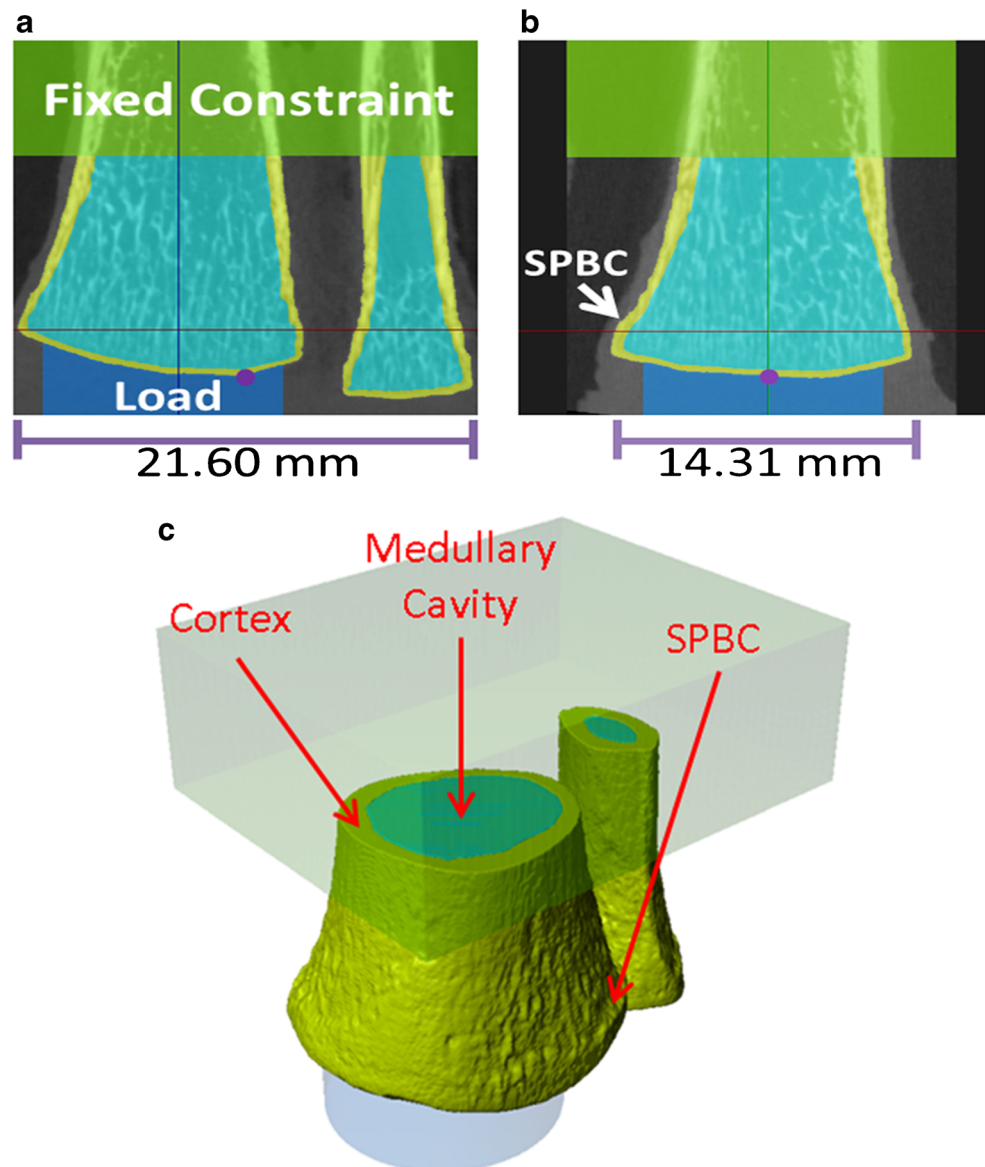
Material properties

Cortical bone has a relatively homogeneous appearance on micro-CT, and thus it was modeled as an isotropic elastic material characterized by Young's modulus and Poisson's ratio. Little data regarding these mechanical properties in infants are available. One experimental study reported the Young's modulus of infant femoral cortical bone to range between 7 and 13 gigapascals (GPa) (mean: 10 GPa) [19]. We chose this mean value as the Young's modulus for both the tibial and fibular cortical bone. For Poisson's ratio of the cortical bone, the most commonly published values range between 0.28–0.33 [20], and we chose 0.3 for both the tibial and fibular cortical bone.

The medullary cavity is traversed by a lattice network of trabecular bone, dominated by longitudinal struts of trabeculae that parallel the mechanical load of the bone. To approximate the biomechanics of this supporting architecture, we modeled the medullary cavity as a transversely isotropic elastic material with a longitudinal axis of

Fig. 2 Geometric model of the normal distal tibia and fibula. The generated coronal (**a**) and sagittal segmentations (**b**) include the cortices and medullary cavities from the reformatted micro-CT data. A fixed constraint is applied in the transparent green region of the image, and the load was applied to the bottom surface of the distal tibial metaphysis via a rigid cylindrical block shown in *blue*. The *purple dot* along the physeal surface of the distal tibial metaphysis denotes the center of rotation for the applied loads, where applicable. The 3-D rendering of this model with the fixed constraint and rigid cylindrical block is shown in (**c**). *SPBC* subperiosteal bone collar

symmetry. Five parameters are required to characterize this transverse isotropy: longitudinal and transverse Young's modulus and Poisson's ratio, and in-plane shear modulus. Knowledge of these mechanical properties in infants is limited. One experimental study showed that the longitudinal elastic modulus of the human tibial medullary cavity is quadratically related with age [21]. Based on the estimated quadratic trajectory, the longitudinal Young's modulus, E_L, was estimated at 252 megapascals (MPa) for a 3-month-old infant. Using sheep data with assumed transverse isotropy of the medullary cavity [22], in conjunction with human-sheep bone maturation relationship [22–24], the ratio of longitudinal to transverse Young's modulus E_L/E_T was estimated at 1.4. This equates to a transverse Young's modulus, E_T, of 176 MPa. For Poisson's ratio of the trabecular bone, the value of 0.3 is commonly employed [25] and was assigned as the longitudinal Poisson's ratio, v_L. Using generalized Hooke's law for a transversely isotropic material ($v_L/E_L = v_T/E_T$), the transverse Poisson's ratio, v_T, was calculated to be 0.21. Finally, by assuming shear isotropy, the shear modulus, G, was calculated to be 97 MPa using the eq. $G = E_L/(2 \times [1 + v_L])$. These material properties were assigned to both the tibial and fibular medullary cavities.

Mesh development

The mesh was created in ScanIP using four-node tetrahedral elements. It consisted of 793,905 elements (270,746 for the tibial cortex; 317,513 for the tibial medullary cavity, 132,712 for the fibular cortex and 72,934 for the fibular medullary cavity). The average volume of each element is 0.0020 mm^3. The nodes from the two different materials were tied to one another along shared boundaries.

Boundary conditions

To systematically investigate potential mechanistic causes of CMLs, our simulations ranged through the spectrum of load scenarios that could cause injury to the distal tibia. Specifically, eight different load scenarios were employed in our finite element simulations: tension, compression, dorsiflexion, plantar flexion, valgus bending, varus bending, internal rotation and external rotation. The proximal ends of the tibia and fibula were fixed in space, and a circular contact surface was specified, centered over the bottom surface of the distal tibial metaphysis, effectively serving as the contact points for the applied load (Fig. 2). Because the bottom surface of the distal tibial has a diameter of approximately 12.76 mm, the diameter of the circular contact surface was empirically set to be smaller at 11.25 mm. By making this contact surface smaller, the artificial strain caused by the direct interface of the applied load to the bone would be entirely

confined to the bottom surface of the distal tibial metaphysis, thus avoiding confounding strains that may extend up along the distal tibial cortex. The 3-D rendering of this model is shown in Fig. 2. The center of rotation for various bending loads (varus bending, valgus bending, internal rotation, external rotation, plantar flexion and dorsiflexion) was specified as the center of the transverse 2-D spatial span (or footprint) of the ankle (purple dot in Fig. 2). For internal and external rotation, the axis of rotation parallels the longitudinal axis of the tibia. For varus and valgus bending, the axis of rotation is an anterior to posterior line that is perpendicular to the longitudinal axis of the tibia. For plantar flexion and dorsiflexion, the axis of rotation is a medial to lateral line that is perpendicular to the longitudinal axis of the tibia. To enable direct comparison across the different load scenarios, the maximum displacement of the contact load surface was arbitrarily set at 1 mm, regardless of the load type. This displacement threshold translated to a 30° internal and external rotation, 30° varus and valgus bending and 51° dorsiflexion and plantar flexion.

Simulations

Strain-based failure criteria have been shown to be more accurate than stress-based failure criteria in identifying bone failure patterns [26, 27]. Therefore, first principal strain was used to identify potential locations of fracture initiation in the tibial cortex. Finite element simulations were performed using COMSOL (COMSOL Inc., Burlington, MA) on a Hewlett-Packard workstation with dual Intel 2.4 GHz Quad-Core processor (Hewlett-Packard Co., Palo Alto, CA).

Parametric study

To evaluate the sensitivity of the above cortical bone and the medullary cavity material property assumptions, parametric simulations were systematically performed under both tension and compression. Specifically, for the cortical bone, the Young's modulus was first varied from 7 GPa to 13 GPa with the Poisson's ratio fixed at 0.3. Then, the Young's modulus was fixed at 10 GPa and the Poisson's ratio was varied from 0.28 to 0.33. For the medullary cavity, the longitudinal Young's modulus, E_L, was varied from 125 MPa to 500 MPa while keeping $E_L/E_T = 1.4$, $v_L = 0.3$ and $v_T = 0.21$. Then, E_L/E_T was varied from 1 to 2 while keeping $E_L = 252$ MPa, $v_L = 0.3$ and $v_T = 0.21$.

Results

The strain patterns associated with each of the various loading conditions are shown in Figs. 3, 4, 5 and 6. The maximum strain of each loading scenario is shown in Table 1.

Fig. 3 Tension and compression. First principal strain distribution of the distal tibia and fibula following tension and compression to the distal tibia, as viewed from anteromedial (*left image set*) and posterolateral (*right image set*) perspectives. A uniform circumferential ring of high strain is shown within the cortex near the subperiosteal bone collar. There is more overall strain with tension than compression. The maximum cortical strains following tension (0.24) and compression (0.15) are along the subperiosteal bone collar. *A* anterior, *L* lateral, *M* medial, *P* posterior
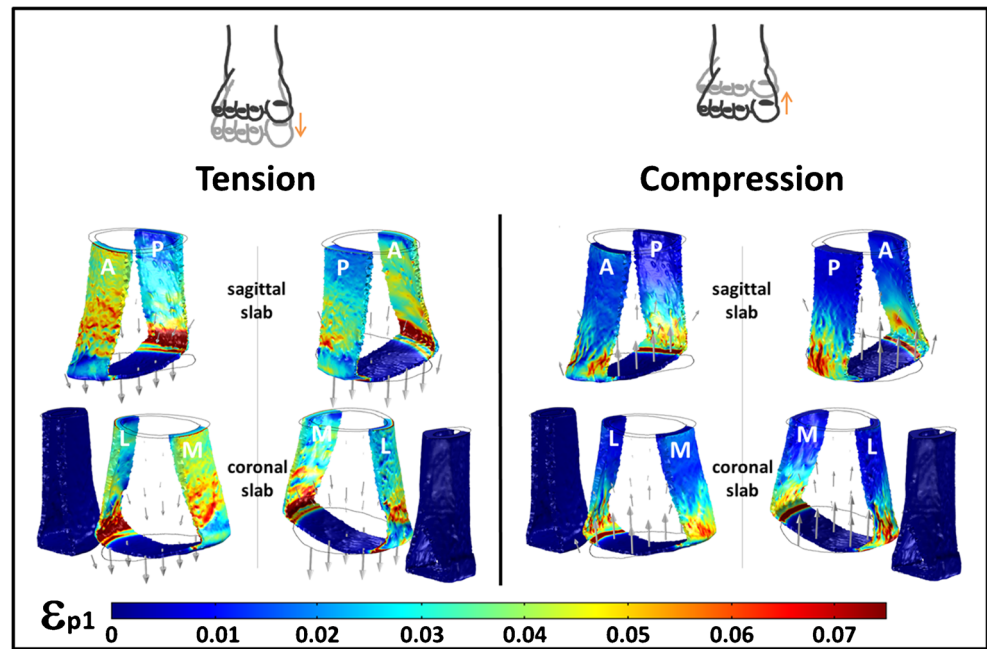
Tension and compression

Tension generated a more uniform distribution of high strain within the cortex near the subperiosteal bone collar (Fig. 3). The strain pattern produced in compression was similar, but 37.5% lower in magnitude. The respective strain patterns infer that the site at-risk of primary cortical bone failure from distal tibial tension and compression would be at the cortex near the subperiosteal bone collar, and that there is a greater risk of injury in tension than compression.

Plantar flexion and dorsiflexion

Plantar flexion resulted in localized areas of high strain along the anterior and posterior aspects of the cortex near the subperiosteal bone collar (Fig. 4). There is a greater degree of strain anteriorly than posteriorly. The strain pattern that results following dorsiflexion is similar to plantar flexion, except there is more strain posteriorly than anteriorly, and the magnitude is increased by 36%. This regional reversal in magnitude is expected given the diametrically

Fig. 4 Plantar flexion and dorsiflexion. First principal strain distribution of the distal tibia and fibula following plantar flexion and dorsiflexion to the distal tibia. Localized areas of high strain are depicted along the anterior and posterior aspects of the cortex near the subperiosteal bone collar. With plantar flexion, greater strain is seen anteriorly than posteriorly. In contrast, with dorsiflexion, greater strain is seen posteriorly than anteriorly. The maximum cortical strains following plantar flexion (0.14) and dorsiflexion (0.22) are along the subperiosteal bone collar. *A* anterior, *L* lateral, *M* medial, *P* posterior
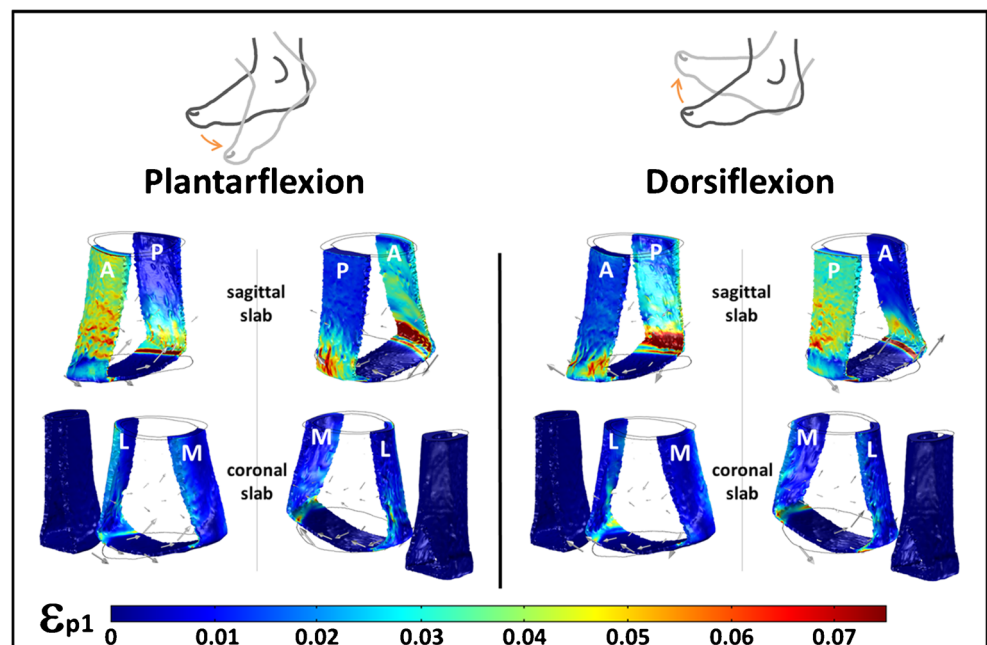
Fig. 5 Varus and valgus bending. First principal strain distribution of the distal tibia and fibula following varus bending and valgus bending to the distal tibia. Localized areas of high strain are depicted along the medial and lateral aspects of the cortex near the subperiosteal bone collar. Though diametrically opposing forces, greater strain is seen medially than laterally for both these loading modalities. The maximum cortical strains following varus (0.08) and valgus (0.10) bending are along the subperiosteal bone collar. *A* anterior, *L* lateral, *M* medial, *P* posterior
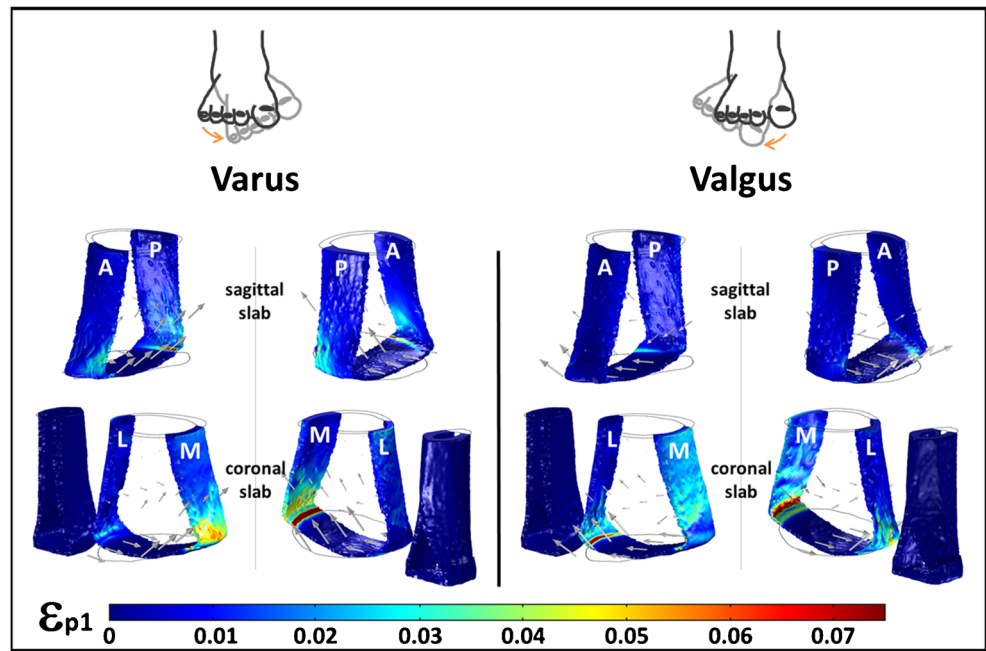
opposite directions of applied force. The focus of the greatest localized strain for both dorsiflexion and plantar flexion directly corresponds to the portion of the cortex under maximal tension. Both these strain patterns suggest that the risk of primary cortical bone failure from plantar flexion and dorsiflexion would be higher at the cortex near the subperiosteal bone collar, and that dorsiflexion poses greater risk of injury than plantar flexion.

Varus and valgus bending

Varus bending resulted in localized areas of high cortical strain along the medial and lateral aspects of the cortex near the subperiosteal bone collar (Fig. 5). There is a greater degree of cortical strain medially than laterally. The cortical strain pattern that results following valgus bending is similar to varus bending, except that the differences in strains medially and

Fig. 6 Internal and external rotation. First principal strain distribution of the distal tibia and fibula following internal rotation and external rotation to the distal tibia. No significant focal or asymmetrical strain is noted in the cortex of the distal tibia. The maximum cortical strains along the distal tibial metaphysis following internal and external rotation are 0.08 and 0.08, respectively. *A* anterior, *L* lateral, *M* medial, *P* posterior
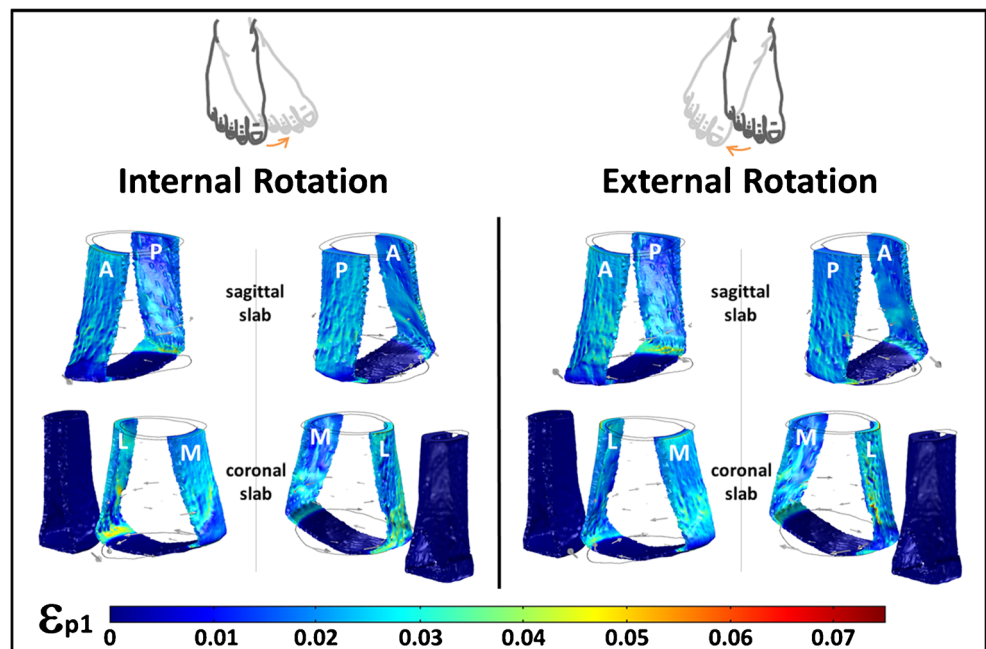
Table 1 Maximum 1st principal cortical strains of the distal tibial metaphysis across different loading conditions

	Tension	Compression	Plantar flexion	Dorsiflexion	Varus bending	Valgus bending	Internal rotation	External rotation
Maximum strain[a]	0.24	0.15	0.14	0.22	0.08	0.10	0.08	0.08

[a] There is no unit associated with strain. Strain is a ratio of two numbers, so it is a dimensionless quantity

laterally are exaggerated. The greatest localized cortical strain for both valgus and varus bending are similar in magnitude (8–10%) and appear to be medial. This is likely explained by the longer lever arm of the medial load surface compared to the lateral surface (relative to the center of rotation), which results in greater medial internal moment. Both of these strain patterns suggest that the risk of primary cortical bone failure of the distal tibia in varus and valgus bending is higher at the cortex near the subperiosteal bone collar.

Internal and external rotation

Little focal or asymmetrical strain was produced with internal or external rotation (8%), and only a small percentage was generated along the distal tibial cortex (Fig. 6). Therefore, neither of these rotations in isolation would likely result in fracture at the subperiosteal bone collar.

Parametric study

Our parametric study showed that changes in realistic ranges of Poisson's ratio and elastic modulus did not alter the patterns but only the magnitudes of strain. Under tension, decreasing the modulus of the cortex to 7 GPa increased the maximum strain by 18% while increasing it to 13 GPa decreased the maximum cortical strain by 11%. Changes to Poisson's ratio only changed the maximum cortical strain by ±1%. Reducing the modulus of the medullary cavity from 252 MPa to 125 MPa decreased the maximum cortical strain by 3%. Doubling the modulus (500 MPa) increased the maximum cortical strain by 37%. Varying E_L/E_T from 1 to 2 only altered the maximum cortical strain by 3–5%.

In compression, varying the modulus of the cortex between 7 and 13 GPa altered the maximum cortical strain by 15%. Varying the Poisson's ratio of the cortex only altered the maximum cortical strain by 1–2%. Decreasing the modulus of the medullary cavity to 125 MPa increased the maximum cortical strain by 13%; while increasing it to 500 MPa decreased the maximum cortical strain by 18%. Decreasing E_L/E_T to 1 decreased the maximum cortical strain by 9%, while increasing it to 2 increased the maximum cortical strain by 7%.

These results suggest that strain magnitudes will vary with material property changes, but the strain patterns will remain the same. The objective of this study was to compare relative magnitudes and strain patterns to identify likely locations of fracture within the cortex under different loading conditions.

Based on the findings of the parametric study, the estimates of material properties used in these simulations are acceptable for this objective.

Discussion

This finite element analysis was undertaken to better understand the biomechanics responsible for CML, a common injury in abused infants. Barber et al. [28] reported a prevalence of 8.5% for CMLs noted on skeletal surveys performed in 567 infant with suspected abuse. This injury constituted 12% of all fractures, and notably, 40% of infants with positive surveys (those with unsuspected fractures) had CMLs. Despite a robust literature attesting to the high frequency and specificity of the CMLs for abuse, the precise mechanism of the injury has proven to be elusive. According to Silverman [29], who interviewed the parents in his 1953 report of three infants with multiple inflicted skeletal injuries, including metaphyseal lesions, the fractures were attributed to tractional forces ("violent jerking") applied to the arms and legs. Caffey [30] considered the metaphyseal fragments "pathognomonic signs of trauma" and invoked the work of Snedecor and Wilson [31] who found similar fractures in infants born by breech extraction. In his subsequent paper on the dangers of infant shaking, Caffey [32] suggested that the metaphyseal fragments resulted from "indirect, traction, stretching, and shearing, acceleration-deceleration stresses" rather than direct impacts.

Several more recent publications support Snedecor and Wilson's findings in breech deliveries, noting fractures resembling CMLs in infants following cesarean section, again suggesting that tractional forces were responsible for the fractures. Valgus and varus bending forces have been used to produce fractures resembling CMLs in cadaveric immature pigs [7, 8], but since there was no histological confirmation of a CML pattern, it is difficult to draw reliable inferences relevant to the mechanisms of inflicted injuries in human infants from these reports.

Our finite element simulations of distal tibial tension, compression, dorsiflexion, plantar flexion, valgus bending and varus bending support the hypothesis that the site of cortical bone failure with the CML is at the margin of the subperiosteal bone collar. In comparing the strain patterns generated across the various normalized load scenarios, tension caused the greatest magnitude and extent of strain, suggesting this type of applied load may require the least amount of effort in the

production of a CML. Tension and compression caused a continuous circumferential ring of high strain along the cortex near the subperiosteal bone collar. In contrast, valgus bending, varus bending, dorsiflexion and plantar flexion resulted in localized areas of strain along the cortex near the subperiosteal bone collar; dorsiflexion resulted in the highest magnitudes of localized strain in this group. Interestingly, valgus and varus bending loads both resulted in higher cortical strains along the medial aspect of the distal tibial cortex near the subperiosteal bone collar, perhaps explaining the tendency for the more focal distal tibial CMLs to involve the medial cortex [33]. Thus, as suggested by Silverman [29], it appears that tensile strains generated by jerking of the lower leg, combined with inversion or eversion of the ankle, could be important biomechanical factors initiating the distal tibial CML.

There are a variety of limitations to this study. First, in an effort to maintain simplicity, we did not attempt to include the distal tibial and fibular physeal/epiphyseal cartilage or ankle ligaments in our finite element model. Histological studies have shown that the distal tibial CML is principally a bony injury without extension to the physis or ligamentous disruption − physeal involvement is seldom seen [12] and ligamentous injury has not been described. We thus made the assumption that any influence of these tissues on the relative strain patterns produced in our simulations would be negligible. Additionally, applying the external load directly to the bony distal tibial metaphysis (instead of indirectly through the epi-physeal cartilage) might affect the resulting strain magnitudes, but the strain patterns should be unaffected. Second, the static finite element analyses performed in this study are only valid in determining probable initial locations of bone failure associated with CML. These simulations do not furnish information about how a cortical fracture propagates into medullary cavity. A quasi-static crack propagation analysis could be performed to simulate such fracture propagation. Third, there is little published data on the material properties of infant cortical and medullary bone, and pediatric elasticity estimates from the density of CT images are questionable [33, 34]. Therefore, we made educated estimates of material coefficients based on adult human data and age-scaling relationships in animals. We believed that small errors in our estimates would be acceptable as they would only affect the magnitude of strain, not the pattern of strain (the focus of our study). This was verified by our parametric study. The inclusion of trabecular structures may alter strain distribution slightly, but independently changing the longitudinal and transverse properties of the medullary cavity had no effect on the strain pattern. Therefore, it is unlikely these structures contribute greatly to cortical strain distribution. Fourth, our geometric model may be somewhat limited as it is based on micro-CT of a single normal specimen. Although modest anatomical variations would likely be encountered if more normal specimens were imaged, the chondro-osseous junction of the infant distal tibia has

undergone many prior radiologic-histopathological studies, and it is reasonable to assume that our material is representative of normal young infant chondro-osseous junction anatomy. Fifth, the depiction of the junction of the subperiosteal bone collar and the adjacent cortex was only roughly approximated in our model. The relatively discrete structure of the subperiosteal bone collar and its thin junction with the adjacent cortex were not fully modeled. Therefore, for the purpose of our experiments, the subperiosteal bone collar and adjacent cortex were considered a single structural unit with the same material properties. Although this is a theoretical limitation of the modeling, we feel this may actually lend support to our finite element analyses. That is, if the thin subperiosteal bone collar/adjacent cortical junction were built into the model, it is likely that the apparent predilection for higher cortical strains at this site would be even greater than we have demonstrated. Finally, our study does not explore Caffey's assertion [32] that the accelerational forces developed during infant shaking alone may be responsible for some CMLs.

Conclusion

This preliminary work suggests that tension, compression, plantar flexion, dorsiflexion, valgus bending and varus bending of the distal tibia can increase the risk of initial cortical bone failure along the margin of the subperiosteal bone collar. Maximum principal cortical strains in this region are greatest with tension and dorsiflexion, and interestingly, focal cortical strains also occur along the medial margin of the subperiosteal bone collar with valgus and varus bending, possibly explaining the known tendency for distal tibial CMLs to occur medially. This modest first step supports the view that the CML fracture is initiated at the margin of the subperiosteal bone collar, but it provides little information with respect to fracture propagation. This study highlights the need for additional clinical and biomechanical data to further explore the biomechanics of this strong indicator of infant abuse.

References

1. Kleinman PK, Perez-Rossello JM, Newton AW et al (2011) Prevalence of the classic metaphyseal lesion in infants at low versus high risk for abuse. AJR Am J Roentgenol 197:1005–1008

2. Strouse PJ, Boal DKB (2013) Child abuse. In: Coley BD (ed) Caffey's pediatric diagnostic imaging. Elsevier, Philadelphia, pp 1587–1598

3. Flaherty EG, Perez-Rossello JM, Levine MA, Hennrikus WL (2014) Evaluating children with fractures for child physical abuse. Pediatrics 133:e477–e489

4. Servaes S, Brown SD, Choudhary AK et al (2016) The etiology and significance of fractures in infants and young children: a critical multidisciplinary review. Pediatr Radiol 46:591–600

5. Ruess L, O'Connor SC, Quinn WJ et al (2003) An animal model for the classic metaphyseal lesion of child abuse. Pediatr Radiol 33:S112

6. Thackeray JD, Wannemacher J, Adler BH, Lindberg DM (2016) The classic metaphyseal lesion and traumatic injury. Pediatr Radiol 46:1128–1133

7. Kleinman PL, Zurakowski D, Strauss KJ et al (2008) Detection of simulated inflicted metaphyseal fractures in a fetal pig model: image optimization and dose reduction with computed radiography. Radiology 247:381–390

8. Thompson A, Bertocci G, Kaczor K et al (2015) Biomechanical investigation of the classic metaphyseal lesion using an immature porcine model. AJR Am J Roentgenol 204:503–509

9. Walsh CJ, Phan CM, Misra M et al (2010) Women with anorexia nervosa: finite element and trabecular structure analysis by using flat-panel volume CT. Radiology 257:167–174

10. Zhang N, Magland JF, Rajapakse CS et al (2013) Assessment of trabecular bone yield and post-yield behavior from high-resolution MRI-based nonlinear finite element analysis at the distal radius of pre-menopausal and postmenopausal women susceptible to osteoporosis. Acad Radiol 20:1584–1591

11. Chang G, Honig S, Brown R et al (2014) Finite element analysis applied to 3-T MR imaging of proximal femur microarchitecture: lower bone strength in patients with fragility fractures compared with control subjects. Radiology 272:464–474

12. Kleinman PK, Marks S (1996) A regional approach to classic metaphyseal lesions in abused infants: the distal tibia. AJR Am J Roentgenol 166:1207–1212

13. Kleinman PK, Marks S, Blackbourne B (1986) The metaphyseal lesion in abused infants: a radiologic histopathologic study. AJR Am J Roentgenol 146:896–905

14. Kleinman PK, Marks S (1995) Relationship of the subperiosteal bone collar to metaphyseal lesions in the abused infants. J Bone Joint Surg 77:1471–1476

15. Kleinman PK, Marks S, Richmond J, Blackbourne B (1995) Inflicted skeletal injury: a postmortem radiologic-histopathologic study in 31 infants. AJR Am J Roentgenol 165:647–650

16. Tsai A, McDonald AG, Rosenberg AE et al (2014) High-resolution CT with histopathological correlates of the classic metaphyseal lesion of infant abuse. Pediatr Radiol 44:124–140

17. Kepron C, Pollanen MS (2015) Rickets or abuse? A histologic comparison of rickets and child abuse-related fractures. Forensic Sci Med Pathol 11:78–87

18. Kleinman PK, Blackbourne BD, Marks SC et al (1989) Radiologic contributions to the investigation and prosecution of cases of fatal infant abuse. N Engl J Med 320:507–511

19. Hirsch C, Evans FG (1965) Studies on some physical properties of infant compact bone. Acta Orthop Scand 35:300–313

20. Shahar R, Zaslansky P, Barak M et al (2007) Anisotropic Poisson's ratio and compression modulus of cortical bone determined by speckle interferometry. J Biomech 40:252–264

21. Ding M, Dalstra M, Kabel J et al (1997) Age variations in the properties of human tibial trabecular bone. J Bone Joint Surg 79:995–1002

22. Nafei A, Danielsen CC, Linde F, Hvid I (2000) Properties of growing trabecular ovine bone. Part I: mechanical and physical properties. J Bone Joint Surg (Br) 82:910–920

23. Kilborn SH, Trudel G, Uhthoff H (2002) Review of growth plate closure compared with age at sexual maturity and lifespan in laboratory animals. Contemp Top Lab Anim Sci 41:21–26

24. Pearce AI, Richards RG, Milz S et al (2007) Animal models for implant biomaterial research in bone: a review. Eur Cell Mater 13:1–10

25. Ulrich D, van Rietbergen B, Weinans H, Ruegsegger P (1998) Finite element analysis of trabecular bone structure: a comparison of image-based meshing techniques. J Biomech 31:1187–1192

26. Schileo E, Taddei F, Cristofolini L, Viceconti M (2008) Subject-specific finite element models implementing a maximum principal strain criterion are able to estimate fracture risk and fracture location on human femurs tested in vitro. J Biomech 41:356–367

27. Li X, Viceconti M, Cohen MC et al (2015) Developing CT based computational models of pediatric femurs. J Biomech 48:2034–2040

28. Barber I, Perez-Rossello JM, Wilson CR, Kleinman PK (2015) The yield of high-detail radiographic skeletal surveys in suspected infant abuse. Pediatr Radiol 45:69–80

29. Silverman FN (1953) The roentgen manifestations of unrecognized skeletal trauma in infants. AJR Am J Roentgenol 69:413–427

30. Caffey J (1957) Some traumatic lesions in growing bones other than fractures and dislocations: clinical and radiological features. Br J Radiol 30:225–238

31. Snedecor ST, Wilson HB (1949) Some obstetrical injuries to the long bones. J Bone Joint Surg 31A:378–384

32. Caffey J (1972) On the theory and practice of shaking infants. Its potential residual effects of permanent brain damage and mental retardation. Am J Dis Child 124:161–169

33. Tsai A, Perez-Rossello J, Breen M, Kleinman P The distal tibial classic metaphyseal lesion: radiographic spatial distribution and biomechanical implications. Pediatr Radiol 47:S157–S158

34. Helgason B, Perilli E, Schileo E et al (2008) Mathematical relationships between bone density and mechanical properties: a literature review. Clin Biomech 23:135–146